Quantitative phase imaging in flows with high resolution holographic diffraction grating

J.M. Desse, Pascal Picart, F. Olchewsky

Quantitative phase imaging in flows with high resolution holographic diffraction grating

Jean-Michel Desse,[1,*] Pascal Picart,[2,3] and François Olchewsky[1]

[1]*ONERA, The French Aerospace Lab, 5, Boulevard Paul Painlevé, F-59045 Lille Cedex, France*
[2]*Université du Maine, CNRS UMR 6613, LAUM, Avenue Olivier Messiaen, F-72085 Le Mans Cedex 9, France*
[3]*École Nationale Supérieure d'Ingénieurs du Mans, rue Aristote, F-72085 Le Mans Cedex 9, France*
[*]*Jean-Michel.Desse@onera.fr*

Abstract: This paper proposes quantitative phase imaging by using a high resolution holographic grating for generating a four-wave shearing interferogram. The high-resolution holographic grating is designed in a "kite" configuration so as to avoid parasitic mixing of diffraction orders. The selection of six diffraction orders in the Fourier spectrum of the interferogram allows reconstructing phase gradients along specific directions. The spectral analysis yields the useful parameters of the reconstruction process. The derivative axes are exactly determined whatever the experimental configurations of the holographic grating. The integration of the derivative yields the phase and the optical thickness. Demonstration of the proposed approach is carried out for the case of the analysis of the supersonic flow of a small vertical jet, 5.56mm in diameter. The experimental results compared with those obtained with digital holography exhibit a very good agreement.

OCIS codes: (090.0090) Holography; (090.1995) Digital holography; (100.3175) Interferometric imaging; (090.2880) Holographic interferometry; (050.1950) Diffraction gratings; (100.5070) Phase retrieval.

References and links

1. C. Mann, L. Yu, C.-M. Lo, and M. Kim, "High-resolution quantitative phase-contrast microscopy by digital holography," Opt. Express **13**(22), 8693–8698 (2005).
2. B. Bhaduri, H. Pham, M. Mir, and G. Popescu, "Diffraction phase microscopy with white light," Opt. Lett. **37**(6), 1094–1096 (2012).
3. V. Chhaniwal, A. S. G. Singh, R. A. Leitgeb, B. Javidi, and A. Anand, "Quantitative phase-contrast imaging with compact digital holographic microscope employing Lloyd's mirror," Opt. Lett. **37**(24), 5127–5129 (2012).
4. N. Lue, J. W. Kang, T. R. Hillman, R. R. Dasari, and Z. Yaqoob, "Single-shot quantitative dispersion phase microscopy," Appl. Phys. Lett. **101**(8), 084101 (2012).
5. H. Pham, B. Bhaduri, H. Ding, and G. Popescu, "Spectroscopic diffraction phase microscopy," Opt. Lett. **37**(16), 3438–3440 (2012).
6. C. Edwards, R. Zhou, S.-W. Hwang, S. J. McKeown, K. Wang, B. Bhaduri, R. Ganti, P. J. Yunker, A. G. Yodh, J. A. Rogers, L. L. Goddard, and G. Popescu, "Diffraction phase microscopy: monitoring nanoscale dynamics in materials science [invited]," Appl. Opt. **53**(27), G33–G43 (2014).
7. P. Girshovitz and N. T. Shaked, "Compact and portable low-coherence interferometer with off-axis geometry for quantitative phase microscopy and nanoscopy," Opt. Express **21**(5), 5701–5714 (2013).
8. G. Rajshekhar, B. Bhaduri, C. Edwards, R. Zhou, L. L. Goddard, and G. Popescu, "Nanoscale topography and spatial light modulator characterization using wide-field quantitative phase imaging," Opt. Express **22**(3), 3432–3438 (2014).
9. P. Ferraro, D. Alferi, S. De Nicola, L. De Petrocellis, A. Finizio, and G. Pierattini, "Quantitative phase-contrast microscopy by a lateral shear approach to digital holographic image reconstruction," Opt. Lett. **31**(10), 1405–1407 (2006).
10. E. Shaffer, C. Moratal, P. Magistretti, P. Marquet, and C. Depeursinge, "Label-free second-harmonic phase imaging of biological specimen by digital holographic microscopy," Opt. Lett. **35**(24), 4102–4104 (2010).
11. H. Gabai and N. T. Shaked, "Dual-channel low-coherence interferometry and its application to quantitative phase imaging of fingerprints," Opt. Express **20**(24), 26906–26912 (2012).
12. A. B. Parthasarathy, K. K. Chu, T. N. Ford, and J. Mertz, "Quantitative phase imaging using a partitioned detection aperture," Opt. Lett. **37**(19), 4062–4064 (2012).
13. P. Picart and M. Malek, "Complex field recovering from in-line digital holography," Opt. Lett. **38**(17), 3230–3232 (2013).

14. J.-M. Desse, P. Picart, and P. Tankam, "Digital three-color holographic interferometry for flow analysis," Opt. Express **16**(8), 5471–5480 (2008).
15. T. Kakue, R. Yonesaka, T. Tahara, Y. Awatsuji, K. Nishio, S. Ura, T. Kubota, and O. Matoba, "High-speed phase imaging by parallel phase-shifting digital holography," Opt. Lett. **36**(21), 4131–4133 (2011).
16. S. Sharma, G. Sheoran, and C. Shakher, "Investigation of temperature and temperature profile in axi-symmetric flame of butane torch burner using digital holographic interferometry," Opt. Lasers Eng. **50**, 1436–1444 (2012).
17. R. Doleček, P. Psota, V. Lédl, T. Vít, J. Václavík, and V. Kopecký, "General temperature field measurement by digital holography," Appl. Opt. **52**(1), A319–A325 (2013).
18. J. M. Desse and P. Picart, "Quasi-common path three-wavelength holographic interferometer based on Wollaston prisms," Opt. Lasers Eng. **68**, 188–193 (2015).
19. J. Primot, "Three-wave lateral shearing interferometer," Appl. Opt. **32**(31), 6242–6249 (1993).
20. J. C. Chanteloup, "Multiple-wave lateral shearing interferometry for wave-front sensing," Appl. Opt. **44**(9), 1559–1571 (2005).
21. P. Bon, G. Maucort, B. Wattellier, and S. Monneret, "Quadriwave lateral shearing interferometry for quantitative phase microscopy of living cells," Opt. Express **17**(15), 13080–13094 (2009).
22. J. Chu and S. W. Kim, "Absolute distance measurement by lateral shearing interferometry of point-diffracted spherical waves," Opt. Express **14**(13), 5961–5967 (2006).
23. Y. S. Ghim, H. G. Rhee, A. Davies, H. S. Yang, and Y. W. Lee, "3D surface mapping of freeform optics using wavelength scanning lateral shearing interferometry," Opt. Express **22**(5), 5098–5105 (2014).
24. K. U. Hii and K. H. Kwek, "Wavefront reversal technique for self-referencing collimation testing," Appl. Opt. **49**(4), 668–672 (2010).
25. W. Lv, H. C. Zhou, and J. R. Zhu, "Implementation of tridirectional large lateral shearing displacement interferometry in temperature measurement of a diffused ethylene flame," Appl. Opt. **50**(21), 3924–3936 (2011).
26. C. Falldorf, "Measuring the complex amplitude of wave fields by means of shear interferometry," J. Opt. Soc. Am. A **28**(8), 1636–1647 (2011).
27. P. Picart and M. Malek, "Digital holographic imaging based on shearing interferometry," FRINGE 2013, The 7th International Workshop on Automatic Processing of Fringe Pattern, Nürtingen, Germany, September 9–11, 2013, pp 745–750.
28. C. Falldorf, M. Agour, and R. B. Bergmann, "Digital holography and quantitative phase contrast imaging using computational shear interferometry," Opt. Eng. **54**(2), 024110 (2015).
29. J. Primot, "Theoretical description of Shack-Hartmann wave-front sensor," Opt. Commun. **222**(1-6), 81–92 (2003).
30. J. Primot and N. Guérineau, "Extended Hartmann test based on the pseudoguiding property of a Hartmann mask completed by a phase chessboard," Appl. Opt. **39**(31), 5715–5720 (2000).
31. D. C. Ghiglia and M. D. Pritt, *Two-dimensional phase unwrapping: theory, algorithms, and software*, (Wiley, 1998).
32. M. P. Rimmer, "Method for evaluating lateral shearing interferograms," Appl. Opt. **13**(3), 623–629 (1974).
33. D. L. Fried, "Least-square fitting a wave-front distortion estimate to an array of phase difference measurements," J. Opt. Soc. Am. **67**(3), 370–375 (1977).
34. R. H. Hudgin, "Wave-front reconstruction for compensated imaging," J. Opt. Soc. Am. **67**(3), 375–378 (1977).
35. J. R. Noll, "Phase estimates from slope-type wave-front sensors," J. Opt. Soc. Am. **68**(1), 139–140 (1978).
36. J. Herrmann, "Least-squares wave-front errors of minimum norm," J. Opt. Soc. Am. **70**(1), 28–35 (1980).
37. W. H. Southwell, "Wave-front estimation from wave-front slope measurements," J. Opt. Soc. Am. **70**(8), 998–1006 (1980).
38. R. Cubalchini, "Modal wave-front estimation from phase derivative meaurements," J. Opt. Soc. Am. **69**(7), 972–977 (1979).
39. K. R. Freischlad and C. L. Koliopoulos, "Modal estimation of a wave front from difference measurements using the discrete Fourier transform," J. Opt. Soc. Am. A **3**(11), 1852–1861 (1986).
40. R. T. Frankot and R. Chellappa, "A method for enforcing integrability in shape from shading algorithms," in *Shape from Shading*, B.K.P. Horn and M.J. Brooks, ed, 89–122 (1989).
41. S. Velghe, J. Primot, N. Guérineau, M. Cohen, and B. Wattellier, "Wave-front reconstruction from multidirectional phase derivatives generated by multilateral shearing interferometers," Opt. Lett. **30**(3), 245–247 (2005).
42. J. Rizzi, T. Weitkamp, N. Guérineau, M. Idir, P. Mercère, G. Druart, G. Vincent, P. da Silva, and J. Primot, "Quadriwave lateral shearing interferometry in an achromatic and continuously self-imaging regime for future x-ray phase imaging," Opt. Lett. **36**(8), 1398–1400 (2011).
43. http://www.ultimate-holography.com/
44. Th. Kreis, *Holographic Interferometry - Pinciples and Methods* (Akademie Verlag series in Optical Metrology Vol. 1, Akademie Verlag Gmbh, Berlin, 1996).

1. Introduction

In the past years, quantitative phase imaging was developed and dedicated to a wide range of applications [1–17]. Phase measurement deals with the optical path length related to propagation inside transparent specimens (transmission illumination) or to reflection on opaque surfaces (reflection illumination), and translates this data into relevant information. A lot of spectacular investigations were demonstrated in biomedical imaging [1–7], topology at

nanoscale and nanoscopy [7,8,13], fluid mechanics [14,15], or measurement of temperatures and thermal exchanges in flames [16,17]. In such approaches, the phase retrieval is based on off-axis architecture (slight tilt between reference wave and probe wave) providing single-shot and real-time capabilities to the technique. Practically, the off-axis property is obtained by adding a spatial carrier frequency to the interferogram/hologram by tilting one of the mirrors of the set-up. The use of an independent reference wave induces sensitivity to external perturbations such as vibrations, temperature exchanges, etc., and leads to an increase in the set-up complexity. Although quite common-path set-ups were proposed [1,3,12,18], another opportunity for the phase evaluation is provided by shearing interferometry [19,20]. It has proven to be efficient for phase measurements in quantitative phase microscopy [21], distance measurement [22], 3D surface mapping [23], optical testing [24], or also temperature measurements [25]. Demonstration of digital holography imaging based on shearing interferometry was also established recently [13,26–28]. The set-up is simplified by eliminating the reference wave and the phase contrast can be measured. Especially, quadri-wave lateral shearing interferometers offer the advantages of being continuously adjustable in sensitivity. In the same way as for off-axis interferometry, the phase is retrieved after a filtering in the Fourier spectrum, and then a spatial integration is required to get the optical wave front [20,29]. The implementation of such an approach may be based on the use of a modified Hartmann mask [29], a chessboard mask [30] or a pure phase mask [13]. The pattern engraved on a substrate produces diffraction orders which interfere to give the shear interferogram. The main drawbacks are related to the complex realization of the mask [30], the temporal fluctuation of the phase mask [13], the parasitic orders [29] and the low resolution of the mask due to the realization process. Note also that with a modified Hartmann mask the parasitic orders can be reduced by using incoherent light [30]. In this paper, the proposed method can be applied using coherent light without suffering from the parasitic orders.

In this paper, we propose an alternative approach for quantitative phase imaging by the use of a high-resolution holographic grating for generating a four-wave shearing interferogram. The high-resolution holographic grating is designed in a “kite” configuration so as to avoid parasitic mixing of diffraction orders. Demonstration of the proposed approach is carried out for the case of the analysis of the supersonic flow of a small vertical jet, 5.56mm in diameter, at 5 bar injection pressure. Comparison with results from both Michelson and “Z” digital holographic configurations exhibits a very good agreement, thus validating the proposed method. So, this paper is organized as follows; in section 2, we describe the theoretical basics and the data processing; section 3 discusses on the realization of the high-resolution holographic grating and section 4 details the experimental set-up that was developed for analyzing the supersonic flow of small vertical jet; in section 5, the quality of the holographic grating is investigated. Section 6 shows experimental results obtained with the proposed approach and gives a comparison with experimental results obtained with other experimental configurations, using a reference wave. Finally, section 7 draws conclusions and perspectives to the study.

2. Theoretical basics

The principle of the phase encoding in a four-wave interferometric mixing is given in Fig. 1. An incident plane wave crosses the test section and it is disturbed by the phenomenon under analysis. Then, the wave is reflected by the beam splitter cube onto a high resolution holographic grating operating in reflection mode. This holographic grating diffracts the useful orders, represented by their wave vectors, onto the recording plane. The different images diffracted by the holographic mirror interfere with each other at a certain distance, δz, of the diffraction plane. The sensor therefore records an interferogram produced by the coherent superimposition of all the diffraction orders. Note that although the common vocabulary for such approach is related to shearing interferometry, the recorded data includes the same amount of information than a digital hologram, as was discussed in [26–28]. Let $A(\mathbf{r}')$ the complex object wave front in the object plane, and $O(\mathbf{r}) = A_O(\boldsymbol{r})\exp(i\varphi_O(\mathbf{r}))$ ($i = \sqrt{-1}$) the wave

front diffracted from the object plane to the recording plane (**r** is the vector of the Cartesian coordinates $\{x,y\}$ in the plane perpendicular to the z direction.

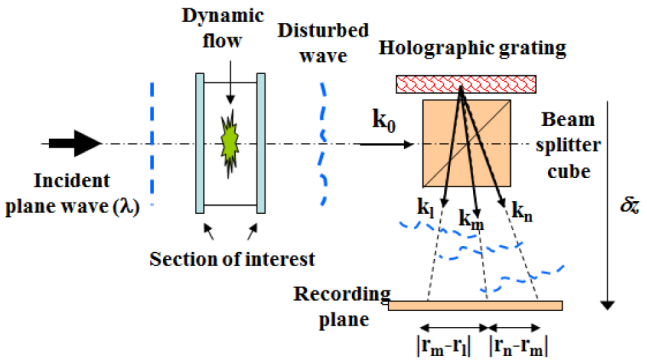

Fig. 1. Principle of wave mixing using a high-resolution reflection hologram.

The reflection of the incident wave on the holographic grating produces a set of replicated waves, which propagation direction is given by their wave vector $\mathbf{k_n} = 2\pi/\lambda\mathbf{e_n}$ ($\mathbf{e_n}$ is the unit vector of the propagation direction). The amplitude of the diffracted wave front at the recording plane is expressed as:

$$O(r,k_n) = A_0(r-r_n)\exp(ik_n.r + i\varphi_0(r-r_n)). \tag{1}$$

In Eq. (1), $\mathbf{r_n}$ is the spatial shift produced by propagation along distance δz from the holographic plane and in the direction of unit vector $\mathbf{e_n}$. Due to the holographic grating, $P = 4$ wave fronts (n varying from 1 to P = 4) are diffracted in different directions. The interferogram recorded in the sensor plane is written as:

$$H(\mathbf{r}) = \sum_{n=1}^{n=P} A_O^2(\mathbf{r}-\mathbf{r_n}) + 2\Re\left\{\sum_{n=1}^{P-1}\sum_{m=n+1}^{P} O(\mathbf{r},\mathbf{k_n})O^*(\mathbf{r},\mathbf{k_m})\right\}. \tag{2}$$

In Eq. (2), the first term is related to the zero order, and the last one is related to coherent cross-mixing between the P diffracted orders. The last term includes the useful data related to the phase at the object plane. Noting $\Delta\varphi_{nm}$ the phase of cross-mixing $O(\mathbf{r},\mathbf{k_n})O^*(\mathbf{r},\mathbf{k_m})$, we get:

$$\Delta\varphi_{nm}(\mathbf{r}) = (\mathbf{k_n}-\mathbf{k_m}).\mathbf{r} + \varphi_O(\mathbf{r}-\mathbf{r_n}) - \varphi_O(\mathbf{r}-\mathbf{r_m}). \tag{3}$$

Equation (3) can be simplified by considering spatial derivatives of the object phase according to:

$$\Delta\varphi_{nm}(\mathbf{r}) \cong (\mathbf{k_n}-\mathbf{k_m}).\mathbf{r} + |\mathbf{s_{nm}}|\frac{\partial\varphi_O(\mathbf{r})}{\partial\mathbf{r}.\mathbf{e_{nm}}}. \tag{4}$$

In Eq. (4), $\mathbf{e_{nm}}$ is the unit vector of vector $\mathbf{s_{nm}} = \mathbf{r_n}-\mathbf{r_m}$ and $(\mathbf{k_n}-\mathbf{k_m}).\mathbf{r}$ is the spatial carrier phase modulation. In the Fourier plane of the interferogram, the diffraction orders are separated from the zero-order diffraction and localized by the spatial frequency vector $(\mathbf{k_n}-\mathbf{k_m})/2\pi$. Since they are localized at different spatial frequencies in the Fourier domain they can be filtered in the same way as for off-axis interferometry. Then, the spatial carrier frequency is removed. Note that spatial derivatives of the object phase are provided along an axis given by the scalar product $\mathbf{r}.\mathbf{e_{nm}}$. The scaling of each spatial derivative is related to $|\mathbf{s_{nm}}|$. Thus, it appears that the method provides spatial derivatives with different sensitivities, which depend on the geometric configuration of the diffraction orders. After extracting each useful order, the term $|\mathbf{s_{nm}}|\partial\varphi_O/\partial\mathbf{r}.\mathbf{e_{nm}}$ is extracted from the argument of the inverse Fourier transform of the filtered interferogram spectrum. We note $\partial\varphi_O/\partial\mathbf{r}.\mathbf{e_{nm}} = \partial\varphi_O/\partial x_q$, $|\mathbf{s_{nm}}| = \alpha_q$ and $D_q = (1/\alpha_q) \times |\mathbf{s_{nm}}|\partial\varphi_O/\partial\mathbf{r}.\mathbf{e_{nm}}$, with q varying from 1 to Q, Q being the number of really independent axis $\mathbf{r}.\mathbf{e_{nm}}$ amongst the set of the useful orders included in the spectrum. So the

spatial variable x_q is simply the direction of the axis along which the derivative operator operates. In the spatial frequency domain, this axis has a corresponding axis which will be referred as u_q. Note that, from a computational point of view, x_q and u_q are 2D vectors. In case that the D_q exceed 2π, phase jumps occur and phase unwrapping is required [31]. The scaling coefficient α_q depends on the distance δz and on the couple of involved wave vectors ($\mathbf{k_n}$,$\mathbf{k_m}$). Then, the spatial integration of terms D_q has to be carried out to get the quantity Ψ. The wave-front reconstruction problem has been discussed by many authors [32–42]. The methods are based on least-squares estimations or modal estimations. As a general rule, fitting is performed by minimizing the mean-square error between the measured differences and the differences according to the estimated wave fronts. A zonal estimation can be also chosen [34–38]. Note that in these works the wave front differences are defined at each point according to the sensor sampling geometry. In the modal approach, the wave front and its differences are expanded in a set of functions and the optimal expansion coefficients are determined (for example, using Zernike and Legendre polynomials). In this paper, the numerical method is based on the weighted least square criterion. According to [13,40,41], quantity Ψ can be recovered by Eq. (5):

$$\Psi = \frac{1}{2i\pi} FT^{-1}\left[\frac{\sum_{q=1}^{Q} u_q \tilde{D}_q}{\sum_{q=1}^{Q} u_q^2}\right]. \tag{5}$$

In Eq. (5), FT means Fourier transform, and $\tilde{D}_q$ is the Fourier transform of D_q. The next section discusses about the holographic grating to get diffraction orders.

3. Design of the high-resolution holographic grating

In order to avoid the drawbacks of the modified Hartmann mask or the pure phase mask, a reflection hologram was designed to produce the suitable diffraction pattern for the four wave shearing interferometric mixing. The reflection grating was encoded on a holographic plate based on a single-layer silver-halide photographic plate [43]. Note that theory on reflection hologram, encoding, transmittance modeling and image formation is well described in [44] which can be considered for further details. The silver grains in the photosensitive layer are sized about 8nm, thus the spatial resolution of the recording material reaches 7,000mm^{-1}. The set-up to record such reflection hologram is described in Fig. 2(a) and uses a continuous laser at λ = 532nm. The input polarization is adjusted by means of the half-wave plate. The acousto-optic cell is used to adjust the exposure time of the hologram.

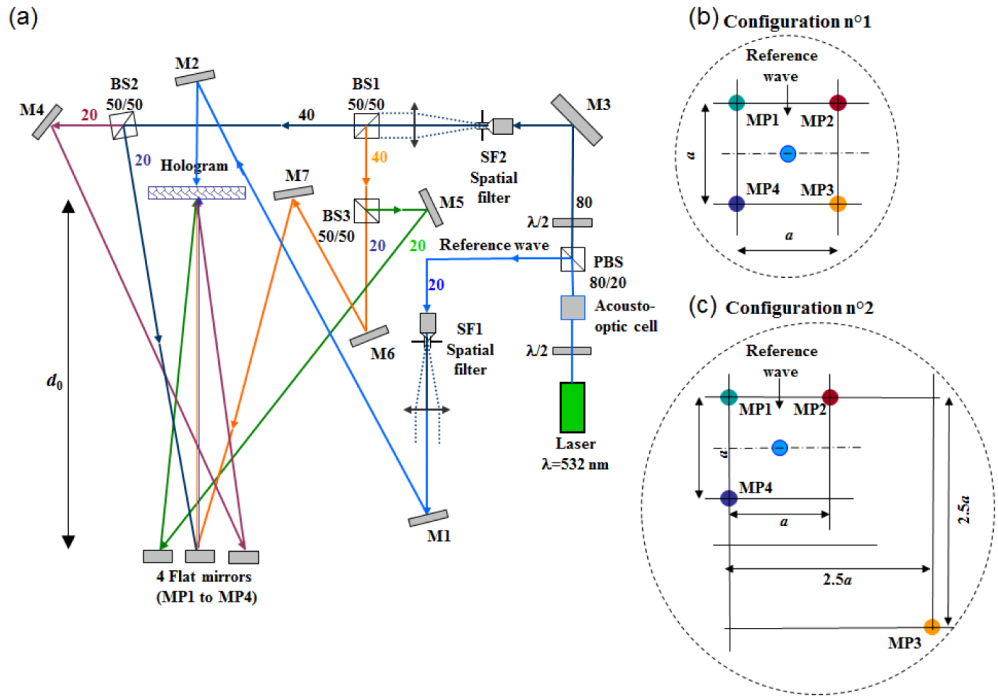

Fig. 2. Optical setup for recording the high-resolution holographic grating in reflection mode (SF1 and SF2: spatial filter, M1 to M7 and MP1 to MP4: flat mirrors, PBS: polarizing beam splitter, BS1 to BS3: 50% beam splitter cube).

A first polarizing beam splitter cube PBS generates a reference beam (blue line) with 20% of the incident light. The 80% of the transmitted light is used to shape four other light beams and its polarization is turned to be parallel to that of the reference beam by using the second half-wave plate. The reference beam illuminates the holographic plate at normal incidence after spatial filtering by SF1 and reflection on mirrors M1 and M2. Fours waves are generated by three beam splitter cubes BS1-BS2-BS3 (50/50) so that the intensity of the five generated beams (the reference beam and the four other waves) is equal to 20% of the optical power at the output of the laser. The set of plane waves is obtained through the spatial filtering provided by SF2. After reflection on several flat mirrors (M4 to M7), four small mirrors reflect each of the beams towards the holographic plate. The beams are impacting the plate with a controlled incidence angle. As the reference wave and the four waves are incoming on each side of the holographic plate, the recorded hologram is a reflection hologram.

Two configurations were tested. The first one (configuration n°1 in Fig. 2(b)) is such that the four mirrors MP1 to MP4 are arranged as a "square" sized $a \times a$. In the second configuration (configuration n°2 in Fig. 2(c)), the square is changed into a "kite" by translating the third corner (mirror MP3) at distance ~$2.5a$ from corners provided by MP2 and MP4. The fours mirrors MP1 to MP4 are localized at distance d_0 from the holographic material.

The hologram has to be recorded sequentially. Indeed, if the hologram was recorded in only one time, that is to say, if the hologram was exposed simultaneously with the reference wave and the four measurement waves, it would register the expected interferences (those in reflection), but also the parasitic interferences in transmission caused by the measurement waves (two by two), and that would drop the diffraction efficiency of the grating. For this reason, The reference wave and one of the four beams are mixed and recording is carried out; then recording of the mixing with the reference wave and another beam is performed; and so on… The time exposure (0.05s) of each individual recording is fixed by the acousto-optic cell. After the four sequential exposures, the holographic plate is chemically processed and

bleached. When illuminating the hologram with a plane wave at normal incidence, four orders are produced by the reflection-mode diffraction. Note that usually a reflection hologram has diffraction efficiency close to 50%. However, by mixing holograms in the holographic material, this diffraction efficiency is reduced: the more the encoded holograms, the lower the diffraction efficiency is. In the present situation, four holograms are recorded in the holographic material. So, the diffraction efficiency obtained along each diffraction order is decreased. Experimentally, we measured diffraction efficiencies at about 2%. The low diffraction efficiency may be balanced by increasing the laser power when illuminating the hologram. With configuration n°1, the diffraction orders have symmetric propagation directions. With configuration n°2, the symmetry is broken since one of the diffracted orders is not included in the corner of the square pattern of configuration n°1 [Figs. 2(b)-2(c)]. The diffraction angles provided by the holographic grating are closely linked to the ratio a/d_0. By simply adjusting distance a, the diffraction angles can be monitored to fulfill the requirements of the optical set-up in which is inserted the component. Note that the "square" configuration is similar to that generally retained for the modified Hartman mask of the pure phase grating.

In the case of using a modified Hartman mask of a spatial light modulator, the resolution of the grating is limited by technology, i.e. lithography process or pixels of the modulator. Since the resolution of the grating is around few microns, the diffraction spectrum calculated from the interferogram included parasitic orders, which reduce the useful spatial bandwidth or may overlap with useful order. In the proposed approach, the holographic grating has a high resolution since the recording process basically is high-resolution (7,000mm^{-1}). It follows that the diffraction pattern does not include parasitic orders and that the spatial bandwidth of the interferogram can be fully exploited. In addition, there is another advantage of the kite configuration. There exists only one couple of interfering waves for each useful order. This leads to an increase of the robustness of the inversion process from spatial derivatives to the real wave front. In the case of classical quadric wave lateral shearing interferometry, the two main useful orders (for the x and y directions) are the spatial average of two couples of interfering waves. Thus, this does not provide more independent derivatives which can be extracted from the processing.

The next section describes the optical set-up in which the high-resolution diffraction grating is inserted, to analyze flows.

4. Experimental set-up for flow analysis

The high-resolution holographic grating is inserted in the optical set-up described in Fig. 3. The set-up is dedicated to the analysis of a small supersonic jet from a nozzle, 5.56mm in diameter. The laser beam at λ = 532nm passes through an acousto-optic cell, is spatially expanded using the spatial filter SF and is collimated with lens L1 (800mm focal length). In Fig. 3, the acousto-optic cell is also used to adjust the exposure time of the hologram. The beam illuminates the test section and crosses once the test section. After passing through and reflection from the mirror M1, the light is directed to the lens set L2-L3, and then travels into the cube BS. The beam is reflected by the beam splitter cube BS1 to the reflection hologram (HRHG). Light is diffracted in reflection mode from HRHG and the diffraction orders are collected by the lens set L4-L5. The lens assembly L2-L3-L4-L5 produces an image of the test section at the sensor plane (1920 × 1440 pixels, sized 3.65μm).

The set of lens L4 and L5 is arranged in a telecentric configuration (afocal configuration) and produces an image of the HGHR at a certain distance δz from the sensor area (refer also to Fig. 1). Noting $G_\alpha = f_4/f_5$ the angular magnification of the lens set L4-L5, a key parameter of the set-up is the diffraction angle $\theta_0 = aG_\alpha/d_0$ which provides the spatial frequency $u_0 = \theta_0/\lambda$ and the spatial shift $\Delta_0 = a\delta z G_\alpha/d_0$ in the sensor plane. The power spectrum density of the interferogram and the shearing quantities of the waves impacting the sensor are closely related to these parameters and to the configuration ("square" or "kite") of the holographic grating recording. In the set-up δz is adjusted to 11.2mm. The next section presents experimental results obtained with the two configurations for the HRHG.

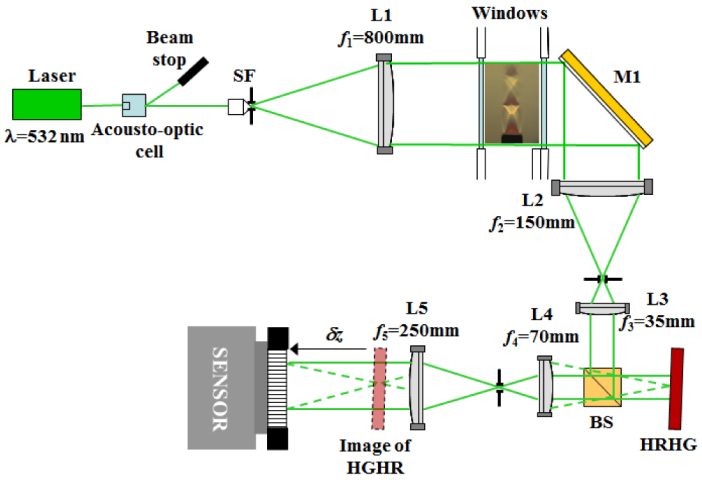

Fig. 3. Set-up for quantitative phase imaging of flows with the holographic grating (SF: spatial filter, L1 to L5: lenses, M1: flat mirror, BS: 50% beam splitter cube; HRHG: high resolution holographic grating).

5. Quality check for the high-resolution holographic grating

In order to evaluate the suitability of the holographic grating for quantitative phase imaging, two reference holograms were recorded without any flow in the test section with holographic gratings recorded with configurations n°1 and n°2. Distance a was adjusted to a = 61mm and d_0 = 1520mm. Figures 4(a) and 4(b) show the experimental configuration for the recording of the grating with mirrors MP1 to MP4. The interfering orders of Eq. (2) are labeled 1 to 4, 1' and 2' in Fig. 4(a) relatively to the interference of waves diffracted from the holographic grating. Then, the spatial frequency spectrums of the interferograms were computed. Figure 4(c) shows the power spectrum for configuration n°1. The spots are labeled according to that in Fig. 4(a) and the axis are increased with reduced spatial frequencies. The energy distribution in the spectrum is quite similar to that obtained in [30]. In this configuration there are Q = 4 useful spectral orders to be processed in Eq. (5). For orders 1,1' q = 1, for 2,2' q = 2, for 3 q = 3, and for 4 q = 4. Considering the symmetry on the diffraction scheme, we have $\alpha_1 = \alpha_2 = \Delta_0$, and $\alpha_3 = \alpha_4 = \sqrt{2}\Delta_0$ for inputs in Eq. (5). Relatively to the spot numbering, the spatial frequencies of the useful spectral orders are $(u_1,v_1) = (u_0,0)$, $(u_1,v_1) = (0,u_0)$, $(u_3,v_3) = (+u_0,-u_0)$, and $(u_4,v_4) = (+u_0,+u_0)$. Figure 4(e) shows the zoom of spectral orders 1,1' in Fig. 4(a). As can be seen, there exist two energy spots close together. However, from a theoretical point of view, these spots should be quite superimposed. This is also the case for spectral orders 2,2'. It appears that the two spectral signatures from on one hand 1 and 1' and on the other hand from 2 and 2' are slightly shifted. Therefore, efficient spatial filtering cannot be performed, inducing a phase mixing when extracting these orders. So the final reconstruction of Ψ cannot be obtained. The main reason to this spectral mixing is related to the slight distance shifts that exist between mirrors MP1 to MP4. It is not possible to separate them for filtering and to reconstruct the phase derivative map induced by only order 1. If the "square" arrangement in Fig. 2(a) is not perfectly realized, then this phenomenon occurs. From an experimental point of view, the perfect square arrangement is not possible since there always exist some deviations to distance a between the four corners. For this reason the recording configuration has to be adapted to avoid the spectral mixing. With the "kite" arrangement of configuration n°2, this mixing has disappeared. Figure 4(b) shows the configuration and the labeling of the spots according to that in Fig. 4(a). In this configuration there are Q = 6 useful spectral orders that can be processed in Eq. (5).

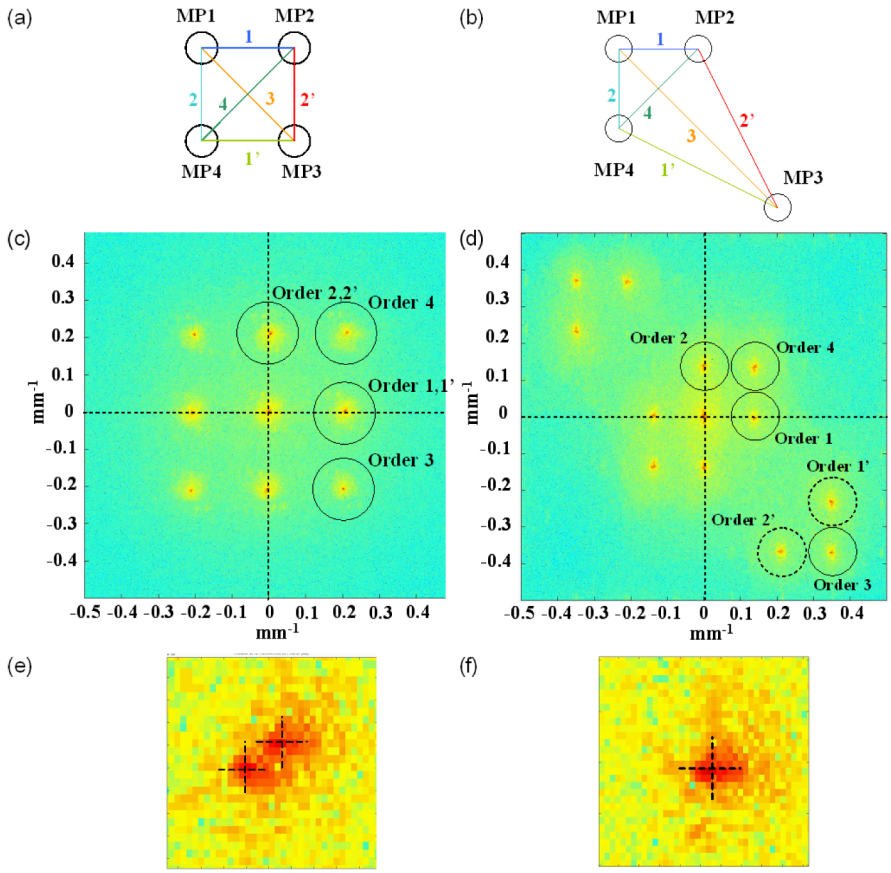

Fig. 4. (a) square configuration with interference labeling, (b) same as (a) for the kite configuration, (c) spatial spectrum for the square configuration, (d) spatial spectrum for the kite configuration with axis increased with reduced spatial frequencies, (e) zoom on the 1,1' spectral order of the square configuration, (c) zoom on the 1 spectral order of the kite configuration.

Figure 4(f) shows a zoom of the + 1 order. As can be observed, there is no spectral mixing since the orders are well separated. Accordingly, the spatial filtering can be efficient and the extracted data can be processed with Eq. (5). The derivative axis x_q (q = 1…6) is related to the position of the diffraction orders in the Fourier spectrum. Each axis is referred to the horizontal axis with an angle γ_q. The spatial frequency coordinates of the peaks yield the angle for each order. From this, the exact derivative axis can be computed as shown in Fig. 5. Considering (u,v), the set of spatial frequencies axis in the Fourier domain, axis u_q is computed with $u_q = \cos(\gamma_q)u + \sin(\gamma_q)v$, for use in Eq. (5). The distance of the peak to the origin of the set of reference axis (u,v) yields the scaling coefficient related to α_q and is proportional to Δ_0. Thus the estimation of the required parameters in Eq. (5) is robust. In addition, the derivative axes are exactly determined, whatever the experimental configurations when recording the reflection holographic grating (corner MP3 in Fig. 2(c) does not require any precise localization).

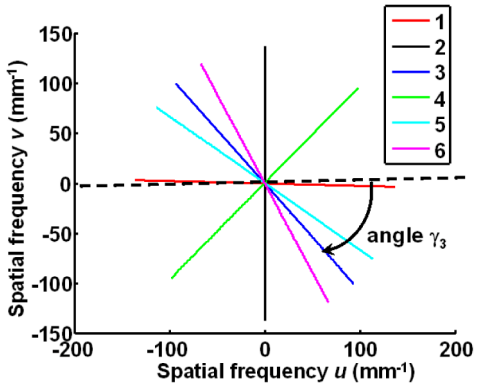

Fig. 5. Derivatives axis in the Fourier domain, each color is related to axis that are numbered 1 to 6; illustration of the angle γ_q with order n°3 and angle γ_3.

Table 1 gives the parameters attached to these spectral orders (α_q,u_q,v_q,γ_q) and the related derivative axis x_q.

Table 1. Parameters of the useful parameters for the "kite" configuration

q	α_q	(u_q,v_q)	Angle γ_q for derivative axis x_q
1	1.0078Δ0	(+ 1.075u0, -0.0249u0)	-1.4144°
2	Δ0	(0, + u0)	90°
3	3.6353Δ0	(+ 2.4813u0,-2.6567u0)	-46.9549
4	1.4021Δ0	(+ 1.0075u0, + 0.9751u0)	44.0655
5	2.9836Δ0	(+ 2.4813u0, -1.6567u0)	-33.7298
6	3.0183Δ0	(+ 1.4776u0, -2.6318u0)	-60.6885

6. Experimental results and comparisons with digital holographic interferometry

This section presents experimental results obtained with the "kite" configuration for the case of the analysis of the supersonic flow of a small vertical jet, at 5bar injection pressure. In order to get quantitative phase imaging of the phenomenon under interest in the test section, the experimental process is as follows: "reference" interferogram (without flow) and "measurement" interferogram (with flow) are recorded by the sensor. First, 2D fast Fourier transform is computed for the reference hologram in order to localize the useful interference orders. The phase is extracted and processed for each selected order. Then, the "measurement" interferogram is processed according to the same scheme. Subtracting the reference data to the measurement data gives a modulo 2π map of the phase gradient difference caused by the flow, for each selected order. Modulo 2π phases are unwrapped before injecting in Eq. (5).

Figures 6(a) and 6(b) show respectively the reference and the measurement interferograms recorded at a pressure of 5bar when δz = 11.2mm. Figure 6(c) shows a zoom of Fig. 6a exhibiting the microscopic fringes of the interferogram. Figures 6(d) to 6(i) show the phase derivatives extracted from the filtering of the useful orders in the interferogram spectrum along derivative axis 1 to 4, 1' [Fig. 6(h)], and 2' [Fig. 6(i)].

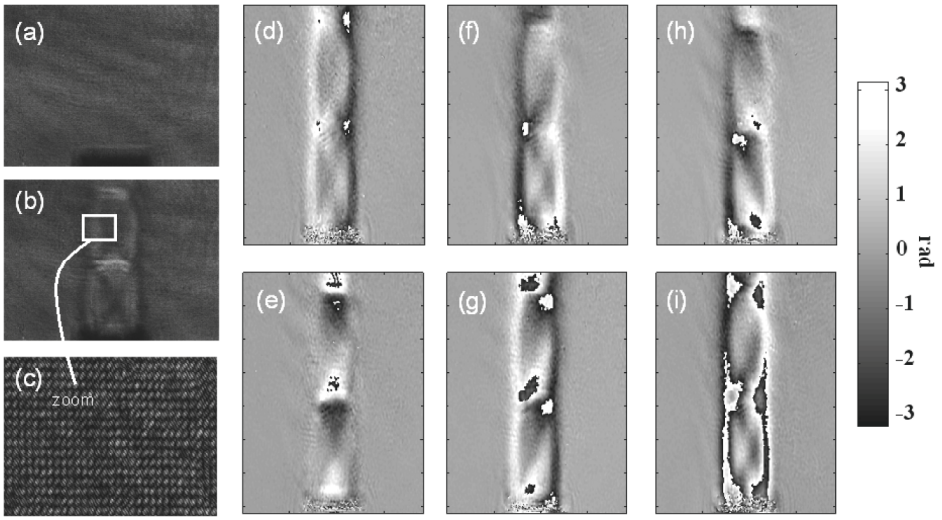

Fig. 6. Recorded interferograms, and maps of modulo 2π phase gradients obtained for the six interference orders, (a) reference interferogram recorded without flow in the test section, (b) interferogram recorded with the micro jet the test section, (c) zoom of the measurement interferogram exhibiting the structure of the microscopic fringes, (d) phase gradient along $q = 1$ (order 1 in Fig. 4(d)), (e) phase gradient along $q = 2$ (order 2 in Fig. 4(d)), (f) phase gradient along $q = 3$ (order 3 in Fig. 4(d)), (g) phase gradient along $q = 4$ (order 4 in Fig. 4(d)), (h) phase gradient along $q = 5$ (order 1' in Fig. 4(d)), (i) phase gradient along $q = 6$ (order 2' in Fig. 4(d)); the gray scale refers to the phase maps.

Each diffraction order in the power spectrum of the interferogram is selected successively and filtered with a circular binary filter with radius $R_u = 10\text{mm}^{-1}$ (reduced spatial frequency at 0.0365mm^{-1}). So, the spatial resolution in the reconstructed image is about 50μm. By using the unwrapped phase gradient differences in the selected derivative directions, the reconstruction of the integrated phase map is possible. For this processing, Eq. (5) is implemented with the useful data. Then, the integrated optical phase is converted into optical thickness. Figure 7(a) shows the optical thickness obtained from the experimental set-up and the use of the 6 useful derivatives extracted from the four-wave mixing interferogram. The fidelity of the measurement can be appreciated by comparing it with those obtained from two other interferometric architectures. These architectures use a reference beam, unlike the proposed method. Figure 7(b) shows the optical thickness measured with a Michelson interferometer in which the test section is crossed twice [14]. This interferometer is sensitive to external perturbations. Figure 7(c) shows the optical thickness measured with a "Z" interferometer based on polarization interferometry and the use of two Wollaston prisms [18]. In this set-up, the test section is crossed only once and the interferometer is quasi-common path set-up, leading to a reduced sensitivity to external perturbations. The color bar for the optical thickness is the same for the three results (maximum at 1.2 μm). Figure 7 shows that spatial locations of the structures of compression and expansion waves are similarly positioned in the three measurements and that they are in good agreement with the knowledge on this topic [18].

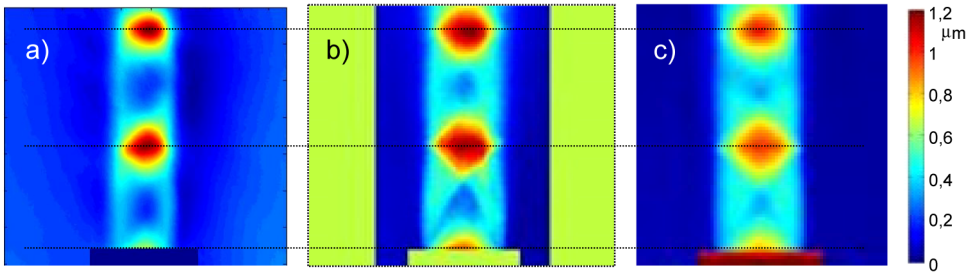

Fig. 7. Comparison of experimental results obtained for three different interferometric techniques for a pressure at P = 5 bars, (a) proposed method, (b) Michelson set-up, (c) "Z" architecture.

7. Conclusion

This paper discusses a shearing interferometric set-up to provide quantitative phase imaging that was applied to analyze flows. The experimental set-up is based on the use of a high resolution holographic grating for generating a four wave shear interferogram. The high resolution holographic grating is designed in a "kite" configuration so as to avoid parasitic mixing of diffraction order. The selection of six diffraction orders in the Fourier spectrum of the interferogram allows reconstructing phase gradients along specific directions. The integration of the phase derivatives yields the absolute phase and the optical thickness. Demonstration of the proposed approach is carried out for the case of the analysis of the supersonic flow of a small vertical jet, 5.56mm in diameter. Experimental results were compared with those obtained with digital holography. First a Michelson set-up, with a twice crossing of the test section, was used, and last "Z" architecture with only one crossing of the test section. The experimental results of the three approaches exhibit a very good agreement. So the proposed approach is able to yield high quality quantitative phase imaging. The reference-free set-up offers a reduce sensitivity to external perturbation and vibrations; in addition, 2D Fourier processing of the interferogram provides a real-time capability to the method. The parameters required for the reconstruction process are robustly evaluated from the spectral analysis. So, the derivative axes are exactly determined whatever the experimental configurations of the reflection holographic grating.

Acknowledgments

The authors thank the French National Agency for Research (ANR) for funding this work under Grant agreement n° ANR-14-ASTR-0005-01.